Wave Equation for Magnetoplasmas in Frequency Domain and Its Zero-Divergence Constraint

Marco Cavenago

Abstract – Radio waves (with angular frequency ω) strongly interact with magnetized plasmas around the electron cyclotron resonance, which, in ion sources or fusion plasma (depending on the DC flux density $\mathbf{B}^s$), is above $\omega/2\pi \geq 10$ GHz, while in the ionosphere, it is about 1 MHz. Minimization of microwave reflection from plasma and radiation from ion sources is important and needs the solution of a vector wave equation whose consistency with boundary conditions is discussed. The plasma modifies the zero-divergence constraint of the electrical field vector, and the solution methods used are revised. An effective criterion to test elliptic problems (even with complex coefficients) is mentioned, applied, and added to graphs. The case of a simplified cylindrical plasma chamber with an extraction cone is discussed; large reflections are sometimes observed as a function of the ratio of plasma angular frequency $\omega_p(z)$ and ω, but regimes with small reflections are also possible; radiation is fairly negligible.

1. Introduction

The interaction of radio waves with magnetized plasma was introduced to explain reflection from the ionosphere [1–3]; among its applications, we find plasma heating in tokamaks (typical frequency $f >$ 100 GHz) and in ion sources (typically $f \cong 20$ GHz). The latter devices may be small (typical plasma chamber radius $R_c < 0.1$ m), so that the free wavelength $\lambda = c/f$ may be comparable with R_c, and wave equation modeling [4], accounting for plasma permittivity $\varepsilon_0 K$ [5, 6], is needed, as discussed also in this article.

In a DC (or static) magnetic flux density $\mathbf{B}^s$, electrons gyrate with angular frequency $\Omega_c = e|\mathbf{B}^s(\mathbf{x})|/m_e$, called cyclotron frequency [5, 7], depending on position $\mathbf{x}$, with $-e$ and m_e the electron charge and mass, respectively. We have the so-called electron cyclotron resonance (ECR), where $\Omega_c \cong \omega = 2\pi f$ with ω the microwave angular frequency; these regions are called ECR layers. In tokamaks, $B^s \cong 6$ T and minor radius $R_c \cong 2$ m, so $f = 170$ GHz and $\lambda/R_c \cong 9 \times 10^{-4}$, while for the ionosphere, $B^s = 0.47$ G, and we may take Earth's radius as a size for R_c, so $f = 1.3$ MHz and $\lambda/R_c = 3.6 \times 10^{-5}$.

To better study resonance effects in ECR ion sources [7], a simplified geometry (with imposed axial symmetry around z) is shown in Figure 1, with input waveguide radius b and ion extraction radius r_h; plasma is confined mostly in a cylindrical chamber $0 < z < L_p$ by a magnetic field. Among design goals of electromagnetic models, we have to minimize the reflection of microwave (back into waveguide) and the radiation from the extraction aperture (or iris) with profiles of plasma electron density $n_e(\mathbf{x})$ and of $B^s(\mathbf{x})$ taken as assigned data. Determination of n_e is the subject of much more complicated modeling [10] and experiments [11]. In our example [12], we set $f = 14.4$ GHz, $R_c = 3$ cm (so $\lambda/R_c = 0.65$), and $L_p = 18$ cm, while r_h may vary (here $r_h = 5$ mm). As a simplifying assumption, we neglect B_x, B_y with respect to B_z, which is reasonable near source axis z; similarly, we neglect the x and y dependence of $n_e(z)$ and $B_z(z)$, which is considered in further studies [13]. Density n_e is related to plasma frequency ω_p by $n_e = m_e\varepsilon_0 (\omega_p/e)^2$, so ω_p and Ω_c can be assigned in place of B^s and n_e. Inside plasma chamber $0 \leq z \leq L_p$, we set

$$\omega_p(z) = \omega\, o_c\, [1 - (z - L_h)^2/L_o^2] \tag{1}$$

$$\Omega_c(z) = \omega\, b_c\, [1 + (z - L_h)^2/L_b^2] \tag{2}$$

with $L_h = L_p/2$; for our typical example, see figure 2 of [6], where $b_c = 0.875$, $L_o = 1.29L_h$, and $L_b = 0.88L_h$. In the waveguide region $z < 0$, $\omega_p(z)$ is smoothly matched down to 0, while Ω_c is taken constant; in the extraction region $z > L_p$, both $\omega_p(z)$ and $\Omega_c(z)$ are smoothly matched to 0. Note that o_c is the central maximum of ω_p/ω. Other plasma resonances may be possible [7–9]; as an example, for $o_c \geq 1$, the longitudinal resonance adds further complexity to ECR. Many valuable results for uniform plasma or specific one-dimensional models exist [14, 15].

The extraction region consists of a cylinder of radius r_h and length z_d joined (see Figure 1a) to a spherical sector with large radius R_s and cone semi-angle θ_{s0}; here, $z_d = 3$ mm, $R_s \cong 4.8\lambda$, and $\theta_{s0} = 4\ \pi/9$.

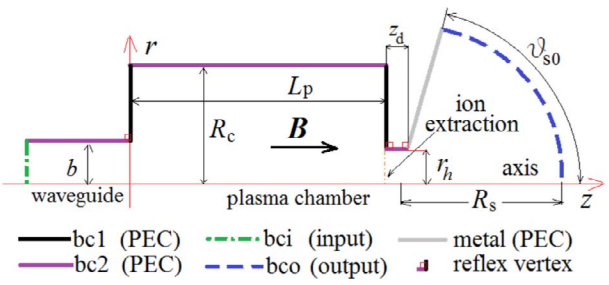

Figure 1. Simplified plasma ion source geometry.

Manuscript received 24 December 2021.

Marco Cavenago is with INFN-Laboratori Nazionali di Legnaro, viale dell'Universitá n. 2, 35020 Legnaro (PD), Italy; e-mail: cavenago@lnl.infn.it.

2. Basic Equations and Conditions

Let $\mathbf{B}^s$ be the static magnetic flux density applied to plasma, $\Re\mathbf{E}(\mathbf{x})e^{i\omega t}$ the radio frequency (rf) electric field, and $\Re\mathbf{B}(\mathbf{x})e^{i\omega t}$ the rf flux density. Assuming $\mathbf{B} = \mu_0\mathbf{H} \ll \mathbf{B}^s$, we can consider that plasma current density $\mathbf{j} \cong \sigma\mathbf{E}$ is approximately a linear functional of the rf field. Thus,

$$\operatorname{curl}\mathbf{H} = \mathbf{j} + i\omega\mathbf{D} = i\omega\varepsilon_0 K \cdot \mathbf{E} \tag{3}$$

where we introduced the effective dielectric tensor $K = I_3 - i\sigma/(\omega\varepsilon_0)$ with I_3 the identity matrix. The plasma conductivity σ is obtained, for a cold plasma [2, 5], from $\mathbf{j} = -n_e e\mathbf{v}$ with $\mathbf{v}$ the average electron velocity satisfying

$$(i\,\omega + \nu)\mathbf{v} = -(e/m_e)(\mathbf{E} + \mathbf{v} \times \mathbf{B}^s) \tag{4}$$

with ν the collision frequency. Typically, $\nu/\omega \ll 1$; note the complex frequency $w = \omega - i\nu$.

Let $x_1x_2x_3$ be a local coordinate system, with $x_3 \,||\, \mathbf{B}^s$; solving (4) for $\mathbf{v}$ and K, we get

$$K = \begin{bmatrix} k_1 & k_2 & 0 \\ -k_2 & k_1 & 0 \\ 0 & 0 & k_3 \end{bmatrix}, \quad \begin{aligned} k_1 &= 1 - (\omega_p^2 w/d_2) \\ k_2 &= -i\omega_p^2\Omega_c/d_2 \\ k_3 &= 1 - \omega_p^2/(w\omega) \end{aligned} \tag{5}$$

with denominator $d_2 = \omega(w^2 - \Omega_c^2)$, which is small at ECR layers $\Omega_c(\mathbf{x}) \cong \pm\omega$.

We now discuss only the electromagnetic part of the problem solution, considering functions K, $\omega_p(z)$, and $\Omega_c(z)$ given. From (3), we get (on the whole simulation domain D_s) the constraint

$$f_c \equiv \operatorname{div} K \cdot \mathbf{E} = 0 \tag{6}$$

for the field combination f_c and the wave equation

$$-\operatorname{curl}\operatorname{curl}\mathbf{E} + (\omega/c)^2 K \cdot \mathbf{E} = 0 \tag{7}$$

Three aspects must match to give a correct problem statement, namely, the equations, the field variables solved for, and the positions where boundary conditions are given. In multiphysics simulation, it is practically convenient to treat E_x, E_y, and E_z as field variables. Solutions (numerical or theoretical) of vector wave equations, which may be more challenging than scalar ones as is well known [4, 16, 17], must preserve constraints as in (6). Moreover, since (in the frequency domain) boundary conditions are given on a closed contour [16, 18, 22], the differential operator must be of elliptic form (which is not obviously satisfied if we consider (7) alone; see also (11)).

It should be noted that (7) can be studied with finite elements more suitable for zero-divergence fields (Nedelec edge elements) or with consistent edge elements [19, 20] instead of the usual Lagrange (or nodal) elements, but some cautions apply [21]; the former elements may give less accurate calculation of derivatives as $E_{x,x}$. It can also be considered to use the divergenceless fields $\check{\mathbf{D}} = K \cdot \mathbf{E}$ as field variables and edge elements for (7) discretization, but this requests the replacement $\mathbf{E} = K^{-1}\check{\mathbf{D}}$ in (7), where the inverse K^{-1} of K has a complicated expression for plasmas [6]. While this choice may be an option for code developers to be investigate further, in this article, we conform to the use of $\mathbf{E}$ as field variables and discuss issues and remedies in this case.

Two independent boundary conditions (bc) are specific to wall kind; for example, at perfectly electric conducting (PEC) walls, the parallel electric field is $\mathbf{E}_{||} = 0$; a third one is

$$f \equiv f_c/k_3 = 0 \tag{8}$$

valid for all walls. Equation 7 has the general form of a second-order partial differential equation $\mathcal{L}\mathbf{E} + \mathcal{B}\mathbf{E} = \mathbf{F}$ for n space dimensions and m field components; $\mathcal{L}\mathbf{E}$ includes second-order derivatives, while $\mathcal{B}$ and $\mathbf{F}$ include all other terms. In detail,

$$\mathcal{L}^i\mathbf{E} = \sum_{j=1}^{m}\sum_{k=1}^{n}\sum_{l=1}^{n} L_{jl}^{ik}(\mathbf{x})E^j_{,kl} \tag{9}$$

with index $i = 1, \ldots, m$ and $a_{,bc}$ a shorthand for partial derivative of a with respect to coordinates b and c (or variables with those indices). The coefficients L_{jl}^{ik} (in general, space dependent) can be tabled as a square matrix L_q^p with index transformations $p = k + (i-1)\,n$ and $q = l + (j-1)n$; new indices p and q run from 1 to $n\,m$.

As is well known, Dirichlet or Neumann boundary conditions on the border of D_s are adequate only if L represents an elliptic operator; L is called elliptic at $\mathbf{x}$ if its characteristic polynomial matrix $L^P(\mathbf{v};\,\mathbf{x})$ satisfies [22]

$$|\det L^P(\mathbf{v};\mathbf{x})| \geq c^1|\mathbf{v}|^{2m}, \quad (L^P)^i_j \equiv \sum_{k=1}^{n}\sum_{l=1}^{n} L_{jl}^{ik}v_k v_l \tag{10}$$

for a constant $c^1 > 0$ with $\mathbf{v}$ a real-valued test vector. For typical applications of complex-valued L, see the image inversion problem [23]. In general, L depends on how the wave equation is written. For Hermitian matrices, a simple elliptic condition is that all eigenvalues have the same sign [22]. For the example of (7), we have $n = 3$, $m = 3$, and the 9×9 matrix

$$L_q^p = \begin{bmatrix} 0 & 0 & 0 & 0 & h & 0 & 0 & 0 & h \\ 0 & 1 & 0 & h & 0 & 0 & 0 & 0 & 0 \\ 0 & 0 & 1 & 0 & 0 & 0 & h & 0 & 0 \\ 0 & h & 0 & 1 & 0 & 0 & 0 & 0 & 0 \\ h & 0 & 0 & 0 & 0 & 0 & 0 & 0 & h \\ 0 & 0 & 0 & 0 & 0 & 1 & 0 & 0 & 0 \\ 0 & 0 & h & 0 & 0 & 0 & 1 & 0 & 0 \\ 0 & 0 & 0 & 0 & 0 & 0 & 0 & 1 & 0 \\ h & 0 & 0 & 0 & h & 0 & 0 & 0 & 0 \end{bmatrix} \tag{11}$$

with shorthand $h = -1/2$. Five eigenvalues of this matrix are 1/2, three are 3/2, and one has value -1, indicating that (11) is not elliptic. Moreover, direct calculation

gives $(L^P)^i_j = |\nu|^2\delta_{ij} - \nu_i\nu_j$ with δ_{ij} the Kronecker delta, so $|\det L^P| = 0$, which confirms that the form of (7) is not elliptic. This conflicts with the convenience of using boundary conditions on a closed contour (and produces unpredictable numerical noise, as observed), but (7) can be modified to solve these issues. First, we show the vacuum case $K = I_3$ for simplicity; the constraint (6) then gives div $\mathbf{E} = 0$ on all the simulation domains and thus grad div $\mathbf{E} = 0$; summing this to (7) results in

$$-\text{curl curl}\,\mathbf{E} + \text{grad div}\,\mathbf{E} \equiv \Delta\mathbf{E} = -(\omega/c)^2\mathbf{E} \qquad (12)$$

thanks to vector operator identities [17]; the coefficient matrix is $L^p_q = \delta_{pq}$, and the characteristic matrix is $(L^P)^i_j = |\nu|^2\delta_{ij}$, so $c^1 = 1$, and (12) is an elliptic partial differential equation.

The plasma case (here studied in 3D coordinates x, y, z or 2D ones r, z and three fields E_r, E_ϑ, and E_z) is far more complicated, but a similar procedure works in most cases. First, $f \equiv f_c/k_3$ satisfies the vector equation

$$-(\omega/c)^2 k_4\mathbf{r}_1 f + \text{grad}\,f = 0, \qquad \mathbf{r}_1 = (x, y, 0) \qquad (13)$$

thanks to (6), with the dimensionless constant k_4 (similar to a Lagrange multiplier) to be chosen later. Summing this to (7), the wave equation can be written as

$$\frac{\omega^2}{c^2}[K\cdot\mathbf{E} - k_4\mathbf{r}_1 f] = \text{curl}^2\mathbf{E} - \text{grad}\,f = -\Delta\mathbf{E} + \text{grad}\,C \qquad (14)$$

with the definition of the scalar $C = \text{div}\,\mathbf{E} - f$. Note that constraint is still included in (14) since, by taking its divergence, we get

$$\frac{\omega^2}{c^2}[k_3 - 2k_4]f - \frac{\omega^2}{c^2}k_4 f_{,r} + \text{div grad}\,f = 0 \qquad (15)$$

For $k_4 > 1$, the term in square brackets is negative with a good margin; thus, by expansion of f in eigenfunctions [24], with boundary condition (8), we get the solution $f = 0$. We set $k_4 = 3$ in the following.

A simple calculation gives

$$C = q_1(E_{x,x} + E_{y,y}) + q_2(E_{y,x} - E_{x,y}) + q_3 E_z \qquad (16)$$

with $q_1(z) = 1 - k_1/k_3$, $q_2(z) = -k_2/k_3$, and $q_3 = -k_{3,z}/k_3$. Note that second derivative of E_z does not appear in grad C and that those of E_y and E_x are multiplied by q_1 or q_2. Since q_1 and q_2 are proportional to ω_p^2, we can expect that the L^P related to (14) is elliptic, at least in underdense plasmas ($\omega_p \ll \omega$), as shown in the following.

Figure 2 shows complex plane λ_c and points $Q_1^d = 1 - q_1(z)$ for several z. For (14), the characteristic polynomial matrix is

$$(L^P)^i_j = |\nu|^2\delta_{ij} - \nu_i w_j \qquad (17)$$

with $\mathbf{w} = (q_1\nu_x - q_2\nu_y,\ q_1\nu_y + q_2\nu_x,\ 0)$. From calculation of det L^P, we can obtain [24]

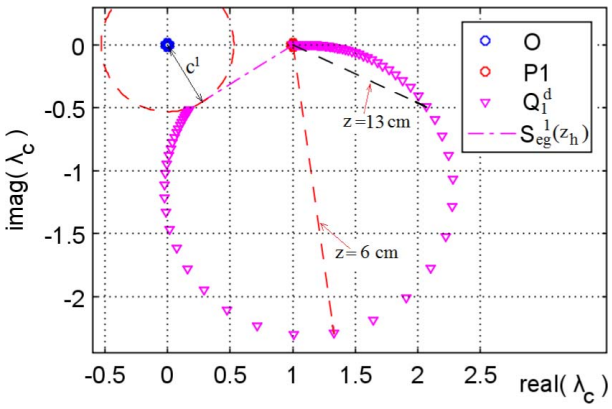

Figure 2. Points $Q_1^d(z)$ in complex plane λ_c for several z and segment S_{eg}^1 for $z_h = L_p/2$ and two other z as labeled, with $L_p = 0.18$ m, $\nu/\omega = 0.06$, and $o_c = 0.5$. Point O is the origin $\lambda_c = 0$, while P1 is $\lambda_c = 1$.

$$c^1 = \min_t |1 - t\,q_1|, \quad t \equiv 1 - (\nu_z/|\nu|)^2 \qquad (18)$$

with the quantity t ranging from 0 to 1, so c^1 is the distance between the $\lambda_c = 0$ point and the line segment S_{eg}^1 joining points 1 and $Q_1^d(z)$. Since $c_1 > 0$ typically for all z (as drawn in Figure 2 for the case $z = z_h = L_h$), (14) is typically elliptic.

Vacuum chamber walls are assumed perfectly (electric) conductive. Details of bc applied to cylindrical symmetry were given elsewhere [6]; for example, we get $E_r = 0$ on "bc1" walls (see Figure 1) and $E_z = 0$ on "bc2" walls; on the input waveguide, we have input condition "bci," with forward wave $\mathbf{E}^+$ parallel to the y-direction on the z-axis; that is, $E_x^+(0, 0, z) = 0$ [6]. Similarly, let $\mathbf{E}^-$ be the backward wave in the waveguide. On generic boundaries (output "bco") with $\mathbf{n}$ the outward normal and no incident field, the matched condition is

$$(\text{curl}\,\mathbf{E})_{\|} = \text{i}k_s\mathbf{E}\times\mathbf{n}, \quad k_s = \mu_0\omega/Z_s \qquad (19)$$

where Z_s is the assumed surface impedance and k_s is called the propagation constant [20]. Using the vacuum impedance $Z_v = \mu_0 c$, we get $k_s = \omega/c$ as usual.

3. Simulation Results

For axial symmetry, components with different azimuthal wavenumber $m_a = 1$ are uncoupled. Figures 3–5 show results of simulations using axial symmetry (2D), restricting to $|m_a| = 1$, as explained in [6], but now including the iris aperture; we set $r_h = 5$ mm. Mesh element size h was kept lower than 0.12λ on the whole domain and smoothly refined down to $h \le 0.02\lambda$ on walls and to $h/\lambda = 3 \times 10^{-3}$ on reflex vertexes; this requests up to 9 GB for a 2D solution, with ample margins for finer meshes in future computations (while 3D solutions seem extremely challenging with similar accuracies). Also, preliminary results for the radiated power fraction $|T|^2$ are shown. Graphs are limited to moderate plasma densities $o_c = \max\ \omega_p/\omega \le 0.9$ (to avoid longitudinal resonances). Since plasma adsorbs

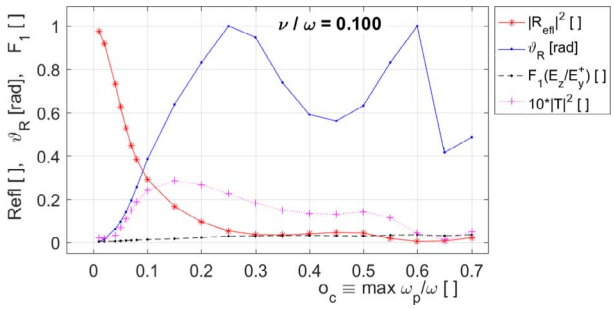

Figure 3. Result summary, at $\nu/\omega = 0.1$ and $b_c = 0.875$, as function of plasma frequency maximum o_c.

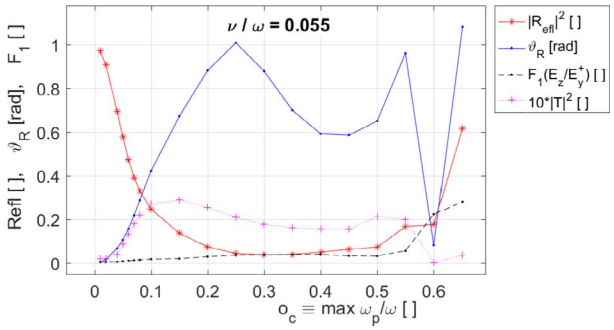

Figure 4. As in Figure 3, but $\nu/\omega = 0.055$.

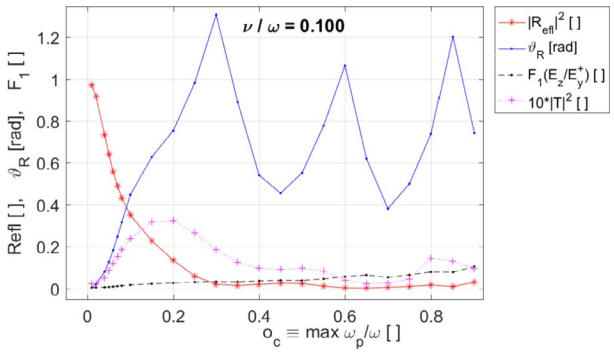

Figure 5. As in Figure 3, but $b_c = 0.97$.

energy before the wave arrives at the iris, $|T|^2$ (approximately estimated by the Poynting vector integral with a 10% error) is typically small; for graph visibility, we multiply $|T|^2$ by 10.

The reflected power fraction, that is, $|R_{eff}|^2 = (|E_x^-|^2 + |E_y^-|^2)/|E_y^+|^2$ into the waveguide, stays below 20% for $0.15 < o_c < 0.7$ for $\nu/\omega = 0.1$, but $|R_{eff}|^2$ becomes larger (even 50%) for $\nu/\omega = 0.055$ and $o_c > 0.6$. From a practical point of view, a reflection of 20% (corresponding to a voltage standing wave ratio of about 2.6) is a tolerable limit since it can be compensated by a tuner before the ion source, while larger reflections may require caution.

An interesting feature (due to plasma and $\mathbf{B}^s$) is the average rotation ϑ_R of the reflected wave, which can also have an E_x component with respect to the injected E_y wave; its definition is $\vartheta_R = \text{atan}(|E_x^-|/|E_y^-|)$ at input. Another important parameter is F_1, the "conversion to E_z" coefficient (ratio of the $|E_z|$ maximum in the plasma chamber to $|E_y^+|$ at input). This stays reasonably small for $\nu/\omega = 0.1$, but rotation ϑ_R can reach values of 1 rad; when reflection is small, ϑ_R can change rapidly since it is then a ratio of small quantities. The lower $\nu/\omega = 0.055$ case (Figure 4) shows enhanced F_1, more ϑ_R fluctuations, and more reflected power for $o_c > 0.5$, consistent with a lower damping of electron motion.

A higher magnetic field case ($b_c = 0.97$, shown in Figure 5) shows small reflection and $|T|^2$, consistent with stronger electron confinement. The rotation ϑ_R of course increases, approaching its $\pi/2$ limit.

In conclusion, radiation from beam aperture was now preliminarily included in our ion source model [6] and is reasonably negligible. The important role of constraint (6) was further demonstrated, in particular for necessary manipulations of the wave equation; the simulation scripts now include tools to verify the wave equation coefficient matrix and its determinant and eigenvalues. In perspective, warm plasma effects will also be considered. The result confirms good absorption of microwaves from cold plasma in typical conditions.

4. References

1. E. V. Appleton, "Wireless Studies of the Ionosphere," *Journal of the Institution of Electrical Engineers*, **71**, 1932, pp. 642-650.
2. E. V. Appleton, "The Influence of the Earth's Magnetic Field on Wireless Transmission," Washington October 1927 Assembly URSI Proceedings, Brussels, Belgium, 1928, pp. 2-3.
3. C. S. Gillmor, "Wilhelm Altar, Edward Appleton, and the Magneto-Ionic Theory," *Proceedings of the American Philosophical Society*, **126**, 1982, pp. 395-440.
4. C. A. Balanis, *Advanced Engineering Electromagnetics*, 2nd Ed., New York, Wiley, 2012.
5. G. D. Swanson, *Plasma Waves*, 2nd Ed., 2003, Bristol, UK, IOP Publishing, 2003.
6. M. Cavenago, "A Simplified Model of Microwave Coupling in ECR Plasmas," 2021 XXXIVth GASS of the URSI, Rome, Italy, September 3, 2021, *IEEE Explore*, doi: 10.23919/URSIGASS51995.2021.9560454.
7. R. Geller, *Electron Cyclotron Resonance Ion Sources and ECR Plasmas*, Bristol, UK, IOP Publishing, 1996.
8. J. Jacquot, V. Bobkov, L. Colas, S. Heuraux, A. Křivskà, et al., "Full Wave Propagation Modelling in View to Integrated ICRH Wave Coupling/RF Sheaths Modelling," *AIP Conference Proceedings*, **1689**, 2015, p. 050008.
9. W. Tierens, D. Milanesio, G. Urbanczyk, W. Halou, V. V. Bobkov, et al., "Validation of the ICRF Antenna Coupling Code RAPLICASOL Against TOPICA and Experiments," *Nuclear Fusion*, **59**, 2019, p. 046001.
10. G. D. Alton and D. N. Smithe, "Design Studies for an Advanced ECR Ion Source," *Review of Scientific Instruments*, **65**, 1994, pp. 775-789.
11. F. Wenander, J. Lettry, and the ISOLDE Collaboration, "MECRIS: A Compact ECRIS for Ionization of Noble Gas Radioisotopes at ISOLDE," *Review of Scientific Instruments*, **75**, 2004, pp. 1627-1629.
12. M. Cavenago, "Modelling Microwave Conversion to Longitudinal Waves in Small ECR Plasmas," *Review of Scientific Instruments*, **67**, 1996, pp. 1079-1081.

13. G. Torrisi, D. Mascali, A. Galatà, G. Sorbello, G. Castro, et al., "Plasma Heating and Innovative Microwave Launching in ECRIS: Models and Experiments," *Journal of Instrumentation*, **14**, 2019, p. C01004.
14. R. S. Brazis and J. K. Furdyna, "Investigation of the Microwave Magnetoplasma Matching Effect in Indium Antimonide," *Journal of Applied Physics*, **48**, 1977, p. 4267.
15. G. Kent, ''Resonant Frequencies and Fields in a Cavity Containing a Magnetoplasma Dielectric," *Journal of Applied Physics*, **39**, 1968, p. 5919.
16. P. M. Morse and H. Feshbach, *Methods of Theoretical Physics*, New York, McGraw-Hill, 1953.
17. J. D. Jackson, *Classical Electrodynamics*, 3rd Ed., New York, Wiley, 1998.
18. I. Babuska, "Error-Bounds for Finite Element Method," *Numerische Mathematik*, **16**, 1971, pp. 322-333.
19. J. C. Nedelec, "Mixed Finite Elements in R^3," *Numerische Mathematik*, **35**, 1980, pp. 315-341.
20. COMSOL, *COMSOL Multiphysics*, version 3.5 (or higher versions), Burlington, MA, COMSOL, http://www.comsol.eu, 2009.
21. G. Mur, "Edge Elements, Their Advantages and Their Disadvantages," *IEEE Transactions on Magnetics*, **30**, 1994, pp. 3552-3557.
22. W. Hackbush, *Elliptic Differential Equations: Theory and Numerical Treatment*, 2nd Ed., Berlin, Springer-Verlag, 2017.
23. J. Valbuena Soler, *Solution of a Second Order Elliptic Partial Differential Equation With Varying Complex Coefficients*, thesis, Australian National University, Canberra, 2017.
24. Wolfram Research, *Mathematica*, version 5.2 (or higher versions), Champaign, IL, Wolfram Research, http://www.wolfram.com, 2005.